Interstitial-Free Bake Hardening Realized by Epsilon Martensite Reverse Transformation

Citation: Wei, Shaolou et al. "Interstitial-Free Bake Hardening Realized by Epsilon Martensite Reverse Transformation." Metallurgical and Materials Transactions A 50, 9 (September 2019): 3985–3991. © 2019 The Minerals, Metals & Materials Society and ASM International

As Published: https://doi.org/10.1007/s11661-019-05344-4

Publisher: Springer Science and Business Media LLC

Persistent URL: https://hdl.handle.net/1721.1/130394

Version: Author's final manuscript: final author's manuscript post peer review, without publisher's formatting or copy editing

Interstitial-Free Bake Hardening Realized by Epsilon Martensite Back Transformation

Cite this article as: Shaolou Wei, Menglei Jiang and Cemal Cem Tasan, Interstitial-Free Bake Hardening Realized by Epsilon Martensite Back Transformation, Metallurgical and Materials Transactions A https://doi.org/10.1007/s11661-019-05344-4

Interstitial-free bake hardening realized by epsilon martensite back-transformation

List of author and affiliation:

Shaolou Wei, lead author

Department of Materials Science and Engineering, Massachusetts Institute of Technology, Cambridge, MA02139, United States of America

E-mail: slwei@mit.edu

Menglei Jiang, contributing author

Department of Materials Science and Engineering, Massachusetts Institute of Technology, Cambridge, MA02139, United States of America

E-mail: mengleij@mit.edu

Cemal Cem Tasan, corresponding author, principal investigator

Department of Materials Science and Engineering, Massachusetts Institute of Technology, Cambridge, MA02139, United States of America

E-mail: tasan@mit.edu

Tel.: 617-253-3318

Interstitial-free bake hardening realized by epsilon martensite back-transformation

Shaolou Wei, Menglei Jiang, and Cemal Cem Tasan*

Department of Materials Science and Engineering, Massachusetts Institute of Technology, Cambridge, MA 02139, U.S.A.

***Corresponding author**: Cemal Cem Tasan (tasan@mit.edu)

Abstract: By investigating a metastable high-entropy alloy, we report a latent strengthening mechanism that is associated with the thermally-induced epsilon-martensite-to-austenite back-transformation. We show this reversion-assisted hardening effect can be achieved in the same time-scale and temperature range as conventional bake-hardening treatment, but leads to both improved strength and cumulative ductility. Key mechanisms are discussed considering transformation kinetics, kinematics, strengthening and ductilization modules.

Keywords: EBSD; metastability; microstructural evolution; in-situ; phase transformation

High-entropy alloys (HEAs) with multi-principal elements have brought about a large degree of freedom in alloy design that can be utilized in the everlasting pursuit for optimal strength-ductility combinations [1,2]. The drastically enlarged compositional space has enabled the activation of multiple strengthening mechanisms [3–7]. Amongst them, strain-induced martensitic transformation is especially effective, promoting strength while simultaneously preserving decent ductility [8]. Thus, both face-centered cubic (FCC) and refractory body-centered cubic (BCC) based metastable HEAs have been designed where significant improvement in mechanical performances were consequently achieved [9,10]. In terms of the FCC-structured metastable HEAs, more recent literature also focuses on providing quantitative design principles, characterizing defect substructure evolution features, and exploring more enhanced properties [11–14].

Although these systematic investigations have advanced the physical insights into the forward FCC austenite-to-hexagonal closed packed (HCP) martensite transformation, the reverse transformation remains comparatively unutilized. To this end, we explore the mechanical property benefits of thermally-induced HCP-martensite-to-austenite reverse transformation in metastable HEAs. The underlying motivations for this study

are two-fold: (1) HCP-martensite has been recognized to possess relatively low thermal stability. Lee et al [15], for example, reviewed that the austenite start temperature (A_s point) decreased monotonically from ~200 to ~150 ^oC as a function of increasing Mn content from 15 to 30 wt.%. Such a low transformation temperature range raises the possibility of feasible thermal processing opportunities similar to bake hardening (BH) treatment, which has not yet been explored; and (2) classical BH treatment in interstitial strengthened Fe- or Al-based alloys involves thermally-assisted segregation of interstitials to dislocation sites, creating a strengthening effect due to the enhanced solute pinning. [16,17]. However, it often inevitably results in cumulative ductility compensation because of the deficiency in dislocation multiplication, leading to the deterioration in strain hardening capability. A bake-reversion treatment that aims at strain-induced martensite reversion, instead of interstitial segregation, should in principle resolve this negative effect.

To explore this processing space, we have exploited an interstitial-free $Fe_{45}Mn_{35}Co_{10}Cr_{10}$ (nominal composition in at. %) HEA as a model system and examined the proposed postulate. Master HEA was fabricated from pure elements through vacuum induction melting followed by hot-rolled to 50 % thickness reduction at 900 ^oC before being homogenized at 1200 ^oC for 2 hrs under argon protection and water-quenched to ambient temperature. Rectangular dog-bone-shaped specimens with gauge geometry of 6.5×2.5×1 mm were sectioned from bulk ingots using electrical discharge machining (EDM) and subsequently subjected to mechanical grinding and polishing to achieve mirror-finish surface condition. Uniaxial tensile experiment was carried out on a Gatan micro-mechanical testing platform at a strain rate of 10^{-4} s^{-1} coupled with digital image correlation technique to acquire local strain information. Microstructural characterizations including morphological observation, electron back-scatter diffraction (EBSD) analysis, energy dispersive X-ray spectroscopy (EDS) study, and electron channeling contrast imaging (ECCI) were performed in a TESCAN MIRA 3 scanning electron microscope (SEM). EBSD data were post-processed in an Orientation Imaging Microscopy (OIM) software, and geometrically necessary dislocation density computation was

accomplished by adopting the algorithm reported by Pantleon [18]. Thermal analysis was conducted for deformed samples (sectioned into 1.5×1.5×0.8 mm small pieces) in a TA Instruments Q100 differential scanning calorimeter (DSC) to determine the A_s and A_f points.

The as-homogenized $Fe_{45}Mn_{35}Co_{10}Cr_{10}$ HEA demonstrates a near-equiaxed grain morphology consisting of FCC-austenite (~95 %) and thermally-induced HCP-martensite (~5 %) phases (Fig. 1 (a)). EDS mapping results confirm that the four principal alloying elements exhibit homogenous compositional distribution. With the occurrence of strain-induced martensitic transformation upon plastic incipience, the metastable $Fe_{45}Mn_{35}Co_{10}Cr_{10}$ HEA shows a desirable strain hardenability, enabling an ultimate tensile strength (UTS) of 568 MPa and a fracture elongation of 0.51 (the dark blue curve in Fig. 1 (b)). Note that the absence of Portevin–Le Chatelier band [19] in Fig. 1 (b) eliminates the contribution of interstitial atoms. The red curve in Fig. 1 (b) reveals a comparative specimen which was pre-deformed to a global strain level of 0.14, unloaded and annealed at 200 ^{o}C for 20 min under high-purity argon protection then re-deformed. Surprisingly, this treated HEA possesses both enhanced strength and cumulative ductility than its as-homogenized counterpart: UTS approaches 627 MPa (10.0 % relative increase) with 0.58 cumulative fracture elongation (15.1 % relative increase). Moreover, the treated HEA exhibits a more moderate drop in strain hardening rate as a function of increasing true strain level, which indicates an enhanced resistance to plastic instability (highlighted by arrows in the inset of Fig. 1 (b)).

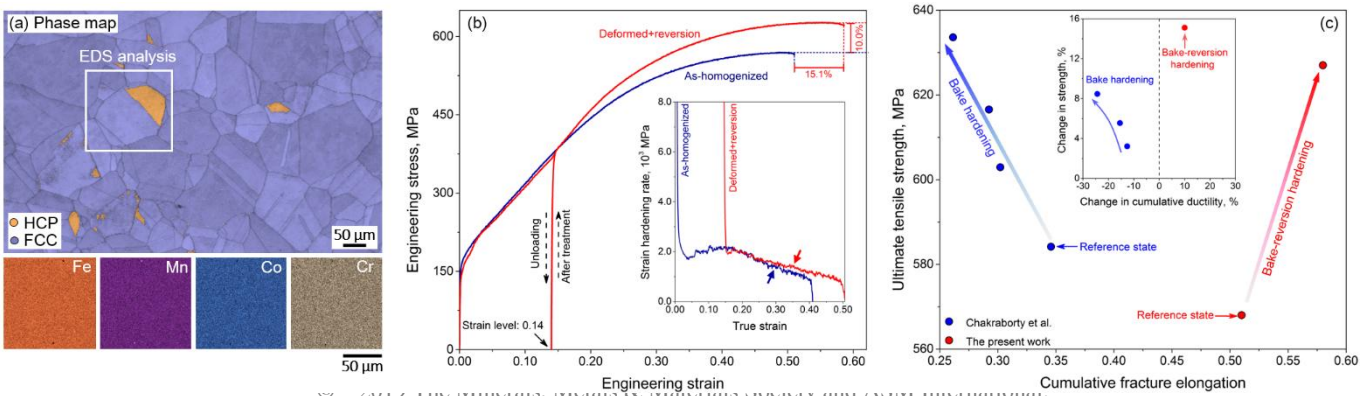

***Fig. 1** | Bake-reversion hardening in a metastable $Fe_{45}Mn_{35}Co_{10}Cr_{10}$ HEA: (a) EBSD phase map of undeformed microstructure corresponded with EDS elemental mapping; (b) engineering stress-strain curves of as-homogenized and bake-reversion treated HEA with strain hardening rate plot inserted; (c) comparison of strength-cumulative ductility synergy between a conventional bake-hardenable Fe-based alloy [16] and the present HEA undergoes bake-reversion hardening.*

Considering the low annealing temperature and similar to the bake hardening treatment, Fig. 1 (c) presents a comparison of the variation in tensile properties with a bake hardenable Fe-based alloy [16] (pre-strained and annealed at 170 ^{o}C for 20 min) that shows a similar UTS value to the present HEA at its reference state. It is recognized that the interstitial-assisted BH mechanism within the Fe-based alloy enables increasing UTS at various pre-strained levels, whereas the cumulative fracture elongation witnesses a monotonic decreasing trend down to 24 % (inset of Fig. 1 (c)). In contrast, concurrent enhancement in UTS and cumulative fracture elongation is achieved in the metastable HEA tested here. Next, we explore the origins of such a latent strengthening module, specifically focusing on the thermally-induced HCP-martensite to austenite reverse transformation.

We first focus on the evolution of phase constitution before and after reversion annealing. As shown in Fig. 2 (a1)-(d1), the parent FCC-phase is mechanically metastable. With increasing local strain level, its fraction decreases from 83 % to 36 % as the local strain level evolves from 0.15 to 0.55 (quantitatively presented in Fig. 3 (a)). This athermic austenite-to-martensite transformation upon deformation not only creates extensive HCP/FCC phase boundaries that suppress dislocation motion but also results in stress delocalization, which as a whole enables the desirable strength-ductility synergy (Fig. 1 (b)). It is recognized from Fig. 2 (a2)-(d2) and Fig. 3 (a) that the 200 ^{o}C 20 min annealing treatment can actually revert strain-induced HCP-martensite back to FCC-austenite. Interestingly, such a reverse austenitic transformation also demonstrates a sensitivity to local pre-strain level: complete reversion (FCC fraction over 99 %) only takes place at a relatively low strain level of 0.15, while a monotonic decreasing trend of FCC fraction is observed with increasing local strain level (Fig. 3 (a)). This sort of dependency can be understood

from the following two aspects: *(1) dislocation plasticity within the strain-induced HCP-martensite.* Unlike the HCP-martensite reported in conventional Co-rich alloys that exhibits a brittle characteristic [20,21], the strain-induced HCP-martensite in the present $Fe_{45}Mn_{35}Co_{10}Cr_{10}$ HEA reveals a c/a ratio of 1.6238 (supplemental information) which indicates a desirable propensity to undergo further plastic deformation after its nucleation. A separate in-situ SEM-based tensile experiment (supplemental information) further demonstrates the presence of slip steps within the strain-induced HCP-martensite, confirming the activation of extensive dislocation plasticity. With elevating local strain level, increasing amount of dislocations will be generated within the HCP-martensite, resulting in the hindered reverse transformation as shown in Fig. 3 (a); and *(2) deformation hardening of untransformed FCC-austenite.* On the other hand, plastic deformation of the FCC phase can either be activated by external loading or associated with the formation of HCP-martensite. Through these two pathways, the untransformed FCC phase will undergo deformation hardening especially at extensive local strain levels (confirmed from low IQ values in Figs. 2 (c2) and (d2)), leading to stronger mechanical suppression to the shear-assisted displacive reverse transformation (see discussion on Fig. 4). The average geometrically necessary dislocation (GND) density within the FCC-austenite (Fig. 3 (b)) preserves almost the same value before and after reversion annealing, indicating negligible recovery softening effect has taken place, which is also confirmed from the invariant yielding point in Fig. 1 (b).

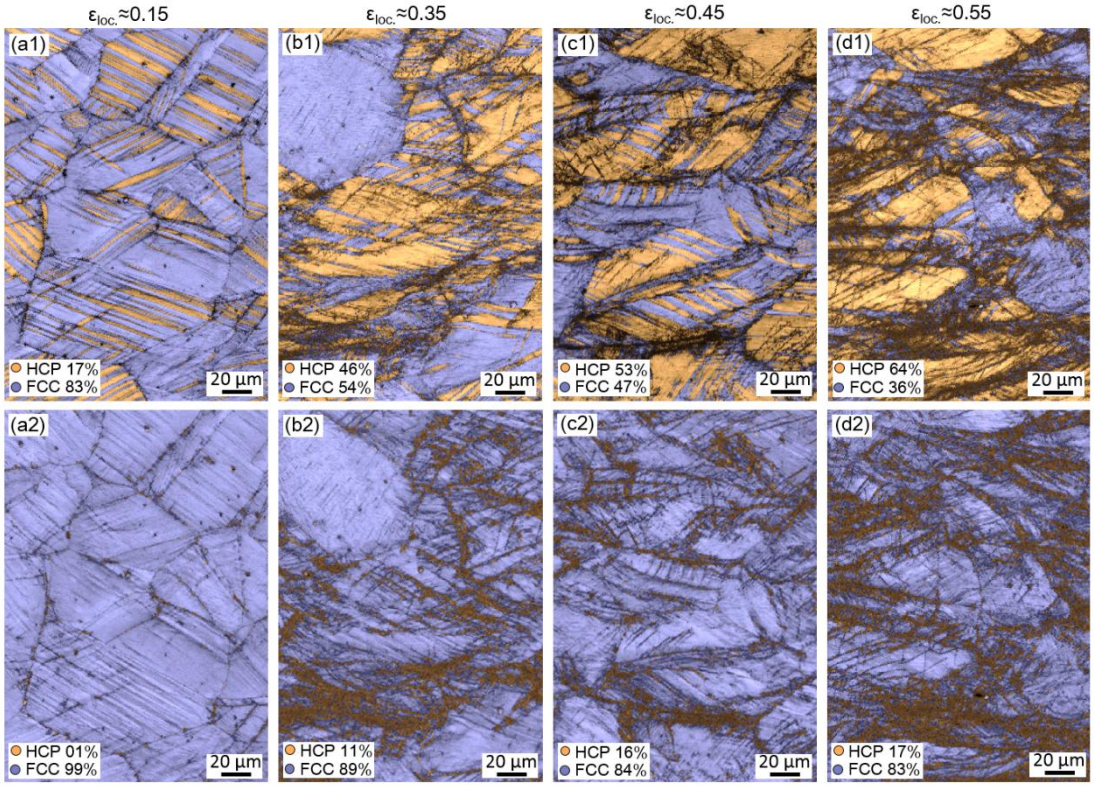

***Fig. 2** | EBSD maps of phase constituent evolution with respect to increasing local strain level (with IQ value overlapped): (a1)-(d2) deformed state; (a2)-(d2) same regimes after 200 °C, 20 min reversion annealing.*

Next, we discuss the reverse transformation kinetics. It has been well-documented in the literature that martensite-to-austenite reverse transformation can exhibit either diffusional or displacive characteristics [22,23]. In the former case, A_s and A_f temperatures were reported to demonstrate elevating trend with respect to increasing heating rate, while in the latter situation, these two characteristic temperatures revealed nearly constant values regardless of heating rate [24]. Fig. 4 (a) shows the DSC results of pre-deformed HEA specimens tested at various heating conditions. All specimens clearly demonstrate endothermic peaks within the temperature range of 160-180 °C, confirming the comparatively low thermal stability of the strain-induced HCP-martensite. The measured A_s and A_f temperatures remain independent to increasing heating rate from 5 °C·min^{-1} to 20 °C·min^{-1} (Fig. 4 (b)), exhibiting only slight decrease as the heating rate reaches 40 °C·min^{-1}. The relatively low transformation temperature, the nearly constant A_s and A_f temperatures, and the composition fully consisting of substitutional alloying elements, all lead to the conclusion that the observed HCP-martensite-to-austenite transformation is accomplished by a shear-assisted

displacive mechanism. The kinematics of this reverse transformation can therefore be understood via the dislocation-based Olson-Cohen model [25]: under external loading, HCP martensite forms due to the $\frac{a}{6} < 112 >$-type mono-directional glide of Shockley partials along every other $\{111\}_{FCC}$ plane. The thermal effect, on the other hand, compensates the activation energy for the backward shearing of these dissociated partials, completing the reverse transformation. Such a shear-assisted displacive mechanism also implies that extensively dislocated HCP-martensite and deformation hardened FCC-austenite will both exhibit more suppression effect on the reverse transformation, which is supportive to the decreasing FCC phase after reversion annealing as a function of increasing local strain level demonstrated in Fig. 3 (a).

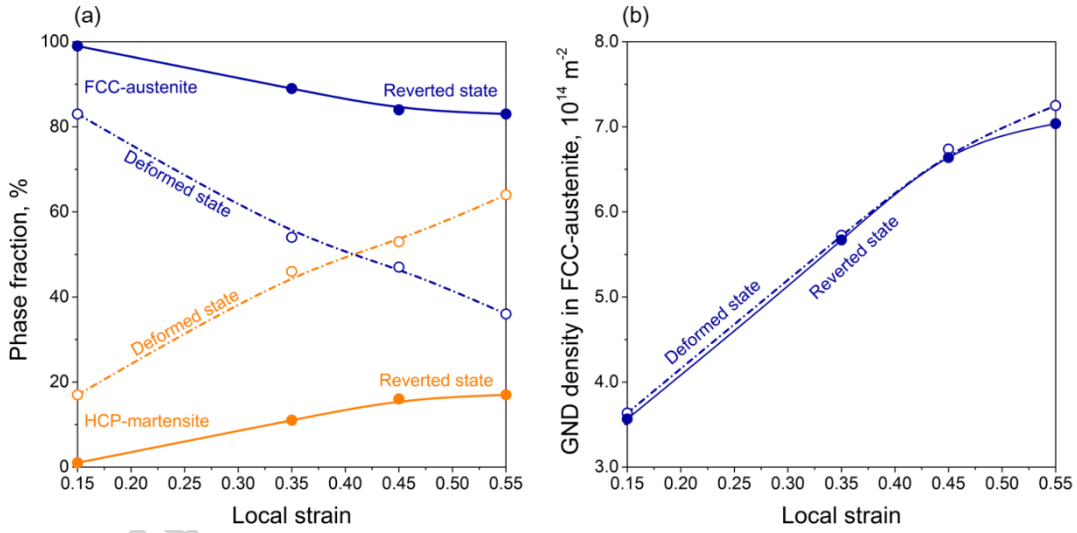

***Fig. 3** | Quantitative assessment of the reverse transformation: (a) phase constitution evolution before and after bake-reversion annealing (dark blue lines: FCC-austenite, orange lines: HCP-martensite); (b) average geometrically necessary dislocation (GND) density versus local strain level within the FCC-austenite (an FCC lattice constant of 3.61 Å measured from synchrotron X-ray diffraction was adopted for the GND density computation).*

We then consider the strengthening and ductilization mechanisms. As mentioned above, the dislocation-based kinematic theory implies the incipience of HCP-martensite formation is a competitive deformation module against perfect dislocation glide [25,26] (dislocation plasticity of parent FCC-austenite). In such a situation, HCP-martensite formation within grain interior usually obeys the mono-variant principle [26], namely nucleates on one of the

$\{111\}_{FCC}$ family planes that exhibits the largest Schmid factor (SF) for the corresponded $\frac{a}{6} < 112 >$-type of partial dislocation shear. Whereas, inverse pole figure (IPF, Fig.4 (a)) taken in a deformed HEA specimen after reversion annealing clearly evidences the formation of secondary HCP-variants (highlighted as A and B in Fig. 5 (a) and (b)).

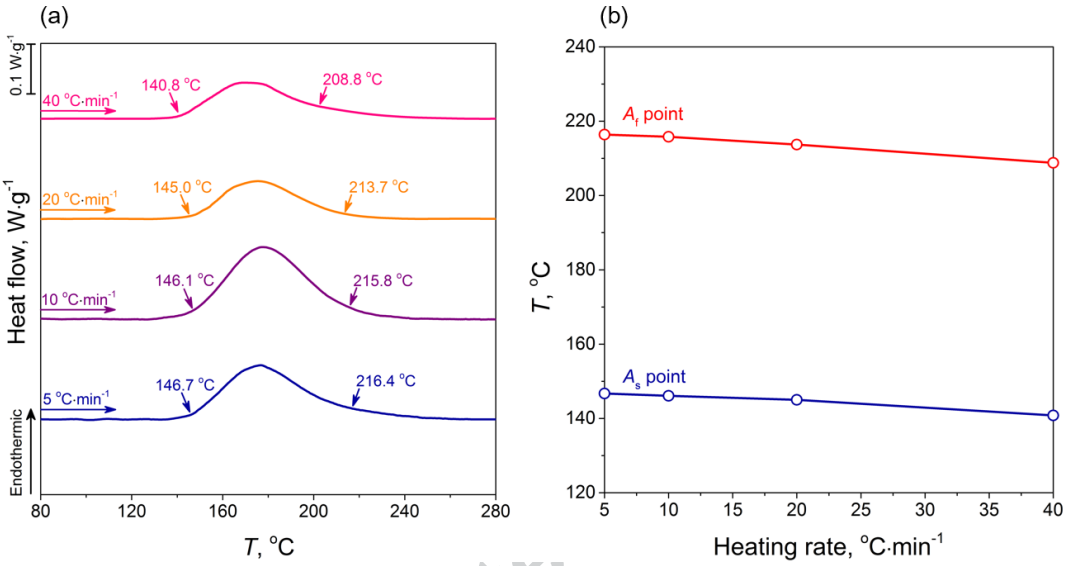

***Fig. 4** | Kinetic features of the reverse transformation: (a) DSC curves at multiple heating rates; (b) measured A_s and A_f temperatures as a function of increasing heating rate.*

We propose a kinematic-energetic model to clarify the formation mechanism of these secondary HCP-variants. The thermally-activated reverse motion of Shockley partials not only gives rise to the reversion transformation but also leads to the formation of emissary dislocations [27,28] jamming along the original FCC/HCP phase boundaries. As schematically depicted in Fig. 6 (a), the existence of one emissary dislocation will result in a localized shear displacement of ϑ of which the corresponding internal shear stress magnitude demonstrates an $\frac{1}{x}$ decay in between the dislocation core and the stress screening regimes [28]. In terms of the strain-induced martensitic transformation, by applying a Legendre transformation, the total Gibbs free energy functional G can be expressed by the addition of internal Helmholtz free energy $F^{int.}$ and external work term:

$$G(T, \varepsilon, x, C) = F^{int.}(T, \varepsilon, x, C) - V(\sigma^{ext.} : \varepsilon) \quad (1)$$

Where T, ε, x, V, and C denote absolute temperature, strain, composition, volume, and other relevant materials constants. In Eq. (1) we employ a linear approximation for the work term, a quadratic approximation for $F^{int.}$, and assume strain-induced martensite formation exhibits an athermic characteristic. We note that since the secondary HCP-variant nucleation evolves plasticity, whereas neither plastic strain nor stress is a state function, we exploit the normalized atomic displacement [29] along the $\frac{a}{6} < 112 >$ direction for secondary HCP-variant formation as the reaction coordinate (x-axis of Fig. 6 (b)). Under this kinematic-energetic framework, the internal Helmholtz free energy of the HEA can be sketched as the grey line in Fig. 6 (b), where the two local minima represent the parent FCC phase and the secondary HCP-variant.

When external loading is applied to an as-homogenized HEA (Fig. 1 (b)), the strain-induced primary HCP-variants tend to follow the Schmid criterion. However, the energy landscape along the secondary $\frac{a}{6} < 112 >$ direction will only be slightly altered, and almost no secondary HCP-variant can form in the grain interior due to the less-preferred energy state (dark blue line marked as "without dislocations" in Fig. 6 (b)). While in the case of a pre-strained and reversion annealed HEA (Fig. 1 (b)), as discussed in Fig. 6 (a), the internal stress field brought about by the large amount emissary dislocations can potentially exhibit a positive shear component in the secondary $\frac{a}{6} < 112 >$ direction, which is in equivalent to providing an extra driving force to the work term in Eq. (1). The net result of this gives rise to a more negative slope in the linearly approximated work term that significantly biases the energy landscape, leading to the energetically favorable nucleation of secondary HCP-variant that even violates the Schmid criterion (red line marked as "with dislocations" in Fig. 6 (b)).

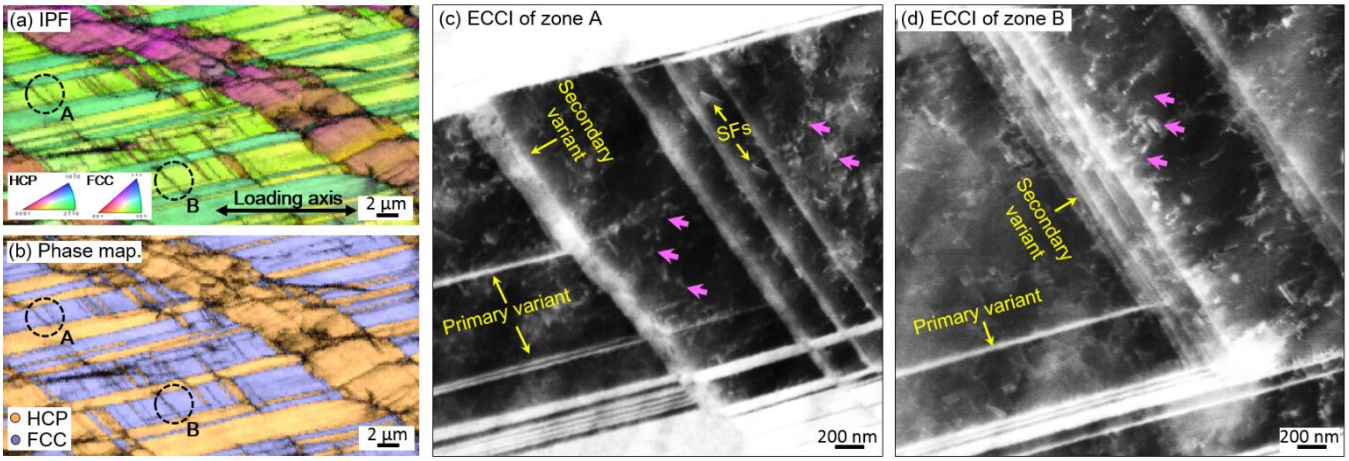

***Fig. 5** | Microstructural characterization of the multi-variant configuration: (a) EBSD IPF map taken at a deformed specimen after reversion treatment (local strain level ~0.30, with IQ value overlapped); (b) phase map correspond to (a); (c) and (d) ECCI micrographs for defect characteristics of regimes A and B marked in (a) and (b) (SF: stacking fault).*

This kind of multi-variant configuration can lead to both strength and cumulative ductility improvement through the following two-fold mechanisms: *(1) improved stress delocalization capability:* As phenomenologically confirmed from the strain hardening rate (inset of Fig. 1 (b)), the reversion annealed HEA exhibits a more moderate decrease in strain hardening rate as deformation proceeds. This implies that the nucleation and growth of the secondary variant facilitates the transformation rate, which adds on to the beneficial effect of reliving local stress concentration and thereby more efficiently promotes deformation homogenization; *(2) enhanced phase boundary-dislocation interactions:* Figs. 5 (c) and (d) reveal the defect characteristics associated with the formation of primary and secondary variants (regimes A and B marked in Fig. 5 (a)). Dislocation pile-ups can be observed near the HCP-martensite plates (highlighted by pink arrows), indicating the strong impingement of mobile dislocation with FCC/HCP phase boundaries. Moreover, the nucleated secondary variant also intersects with the primary variant, which drastically decreases the mean free path of perfect dislocation glide, contributing to the increased UTS achieved within the bake-reverted HEA (namely, an expedited dynamic Hall-Petch effect).

The microstructure development resulting from pre-straining, bake-reversion annealing, and final straining can be summarized as Fig. 6 (c1)-(c4). In a mechanically metastable HEA, the strain-induced FCC-austenite to HCP-martensite transformation is stimulated upon pre-straining (Figs. 6 (c1)-(c2) and 2 (a1)-(d1)). Due to the relatively low thermal stability of the strain-induced HCP-martensite, a 200 ^{o}C, 20 min baking treatment can activate a shear-assisted displacive HCP-to-FCC reverse transformation (Figs. 6 (c3), 2 (a2)-(d2), and 4 (b)), leaving behind emissary dislocations (dashed-line in Fig. 6 (c3)) along the original FCC/HCP phase boundaries. This sort of bake reversion annealing treatment facilitates the nucleation of secondary HCP-variant that intersects with primary HCP-variant upon further loading (Fig. 6 (c4)), which contributes to the simultaneous enhancement in strength and cumulative ductility (Figs. 1 (b) and (c)).

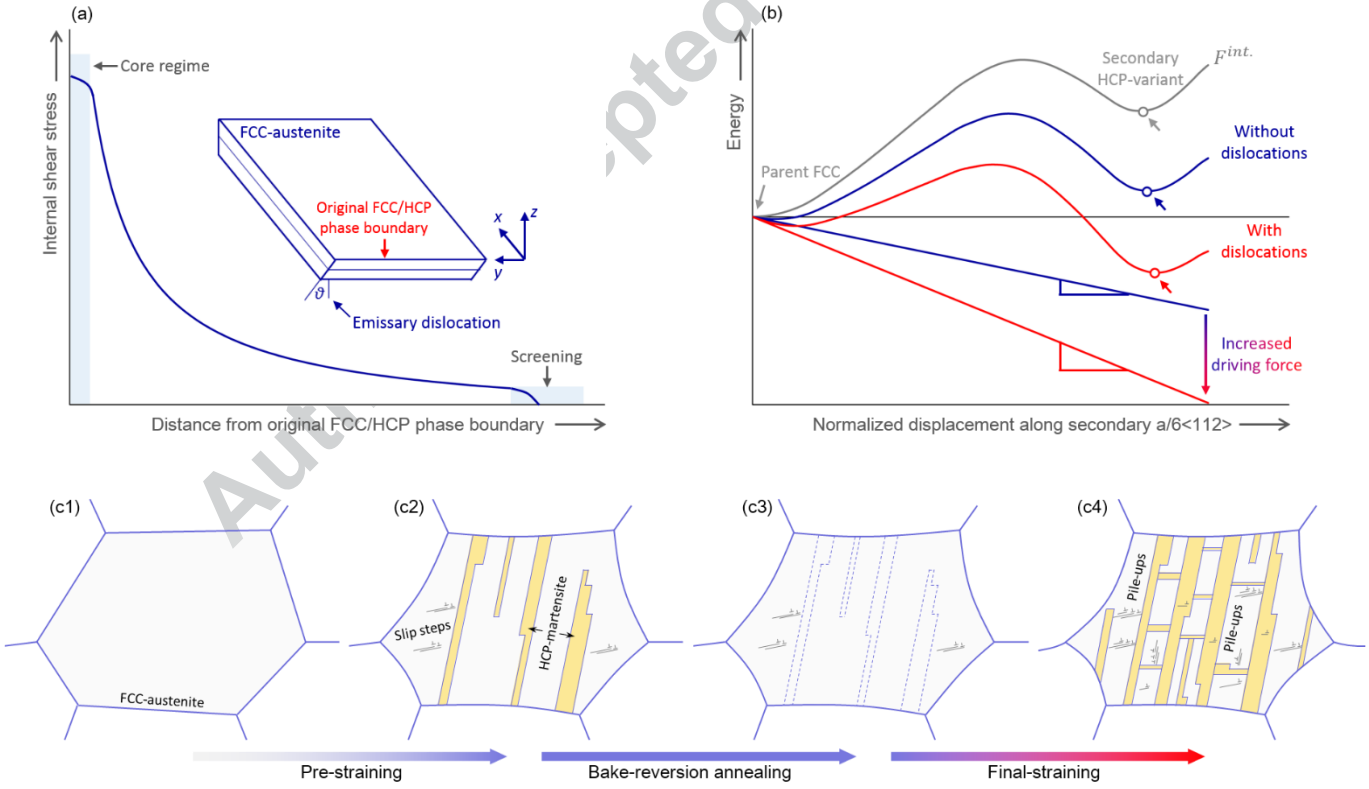

***Fig. 6** | Kinematic-energetic model for secondary HCP-variant formation and the corresponding strengthening and ductilization mechanisms: (a) internal stress field generated by an emissary dislocation at the original FCC/HCP phase boundary; (b) energy landscape of dislocation-assisted secondary HCP-variant formation (y-axis can also be regarded as generalized stacking fault energy [29,30]); (c1)-(c4) phenomenological model elucidating the mechanisms of bake-reversion hardening.*

In summary, we introduce here a latent strengthening mechanism that can be achieved in alloys that exhibit strain-induced HCP-martensite transformation, by accomplishing thermally-assisted HCP-martensite-to-austenite reverse transformation. It is recognized that this kind of reverse transformation exhibits a displacive characteristic that can be activated at a relatively low temperature close to the traditional BH treatment regime for a short period, but results in a simultaneous improvement in both strength and cumulative ductility. The mechanical tests, EBSD, and ECCI-based microstructural analyses suggest that the bake-reversion hardening effect can be attributed to the improved stress delocalization capability and the enhanced phase boundary-dislocation interaction, which simultaneously brought about by the nucleation of secondary HCP-martensite variant.

Acknowledgements

The authors thank Ms. Geetha Berera for extensive support on the DSC measurement. Dr. Hyunseok Oh and Ms. Yuntong Zhu are also acknowledged for fruitful discussion and important inputs. Shaolou Wei would like to express his gratitude to Prof. Ju Li (Massachusetts Institute of Technology, U.S.A.) for the valuable suggestions on energy landscape.

References

1 J.W. Yeh, S.K. Chen, S.J. Lin, J.Y. Gan, T.S. Chin, T.T. Shun, C.H. Tsau, and S.Y. Chang: *Adv. Eng. Mater.*, 2004, vol. 6, pp. 299–303.

2 B. Cantor, I.T.H. Chang, P. Knight, and A.J.B. Vincent: *Mater. Sci. Eng. A*, 2004, vol. 375–377, pp. 213–8.

3 S. Antonov, M. Detrois, and S. Tin: *Metall. Mater. Trans. A Phys. Metall. Mater. Sci.*, 2018, vol. 49, pp. 305–20.

4 F. He, Z. Wang, Q. Wu, J. Li, J. Wang, and C.T. Liu: *Scr. Mater.*, 2017, vol. 126, pp. 15–9.

5 C. Varvenne, A. Luque, and W.A. Curtin: *Acta Mater.*, 2016, vol. 118, pp. 164–76.

6 Z. Lei, X. Liu, Y. Wu, H. Wang, S. Jiang, S. Wang, X. Hui, Y. Wu, B. Gault, P. Kontis, D. Raabe, L. Gu, Q. Zhang, H. Chen, H. Wang, J. Liu, K. An, Q. Zeng, T.G. Nieh, and Z. Lu: *Nature*, 2018, vol. 563, pp. 546–50.

7 H.S. Oh, D. Ma, G.P. Leyson, B. Grabowski, E.S. Park, F. Kormann, and D. Raabe: *Entropy*, 2016, vol. 18, pp. 1–9.

8 S. Wei, F. He, and C.C. Tasan: *J. Mater. Res.*, 2018, vol. 33, pp. 2924–37.

9 Z. Li, K.G. Pradeep, Y. Deng, D. Raabe, and C.C. Tasan: *Nature*, 2016, vol. 534, pp. 227–30.

10 H. Huang, Y. Wu, J. He, H. Wang, X. Liu, K. An, W. Wu, and Z. Lu: *Adv. Mater.*, 2017, vol. 29, pp. 1–7.

11 Y. Ikeda, F. Körmann, I. Tanaka, and J. Neugebauer: *Entropy*, 2018, vol. 20, p. 655.

12 S. Wei, J. Kim, and C.C. Tasan: *Acta Mater.*, 2019, vol. 168, pp. 76–86.

13 S.S. Nene, M. Frank, K. Liu, R.S. Mishra, B.A. McWilliams, and K.C. Cho: *Sci. Rep.*, 2018, vol. 8, pp. 1–8.

14 D. Wei, X. Li, W. Heng, Y. Koizumi, F. He, W.-M. Choi, B.-J. Lee, H.S. Kim, H. Kato, and A. Chiba: *Mater. Res. Lett.*, 2018, vol. 7, pp. 82–8.

15 Y.K. Lee and C.S. Choi: *Metall. Mater. Trans. A*, 2000, vol. 31, pp. 355–60.

16 A. Chakraborty, M. Adhikary, T. Venugopalan, V. Singh, T. Nanda, and B.R. Kumar: *Mater. Sci. Eng. A*, 2016, vol. 676, pp. 463–73.

17 Y. Aruga, M. Kozuka, Y. Takaki, and T. Sato: *Metall. Mater. Trans. A Phys. Metall. Mater. Sci.*, 2014, vol. 45, pp. 5906–13.

18 W. Pantleon: *Scr. Mater.*, 2008, vol. 58, pp. 994–7.

19 R.E. Reed and A.S. Gijilec: *Metall. Trans. A*, 1975, vol. 6, pp. 461–6.

20 D. Wei, A. Anniyaer, Y. Koizumi, K. Aoyagi, M. Nagasako, H. Kato, and A. Chiba: *Addit. Manuf.*, 2019, vol. 28, pp. 215–27.

21 K. Ueki, K. Ueda, M. Nakai, T. Nakano, and T. Narushima: *Metall. Mater. Trans. A Phys. Metall. Mater. Sci.*, 2018, vol. 49, pp. 2393–404.

22 Y. Lü, B. Hutchinson, D.A. Molodov, and G. Gottstein: *Acta Mater.*, 2010, vol. 58, pp. 3079–90.

23 A. Kisko, A.S. Hamada, J. Talonen, D. Porter, and L.P. Karjalainen: *Mater. Sci. Eng. A*, 2016, vol. 657, pp. 359–70.

24 J. Han and Y.K. Lee: *Acta Mater.*, 2014, vol. 67, pp. 354–61.

25 G.B. Olson and M. Cohen: *Metall. Trans. A*, 1976, vol. 7, pp. 1897–904.

26 J.R. Patel and M. Cohen: *Acta Metall.*, 1953, vol. 1, pp. 531–8.

27 S. Kajiwara and T. Kikuchi: *Philos. Mag. A Phys. Condens. Matter, Struct. Defects Mech. Prop.*, 1983, vol. 48, pp. 509–26.

28 P.M. Anderson, J.P. Hirth, and J. Lothe: *Theory of Dislocations 4th Edition*, 2017.

29 S. Ogata, J. Li, and S. Yip: *Phys. Rev. B - Condens. Matter Mater. Phys.*, 2005, vol. 71, pp. 1–11.

30 V. Vítek: *Philos. Mag.*, 1968, vol. 18, pp. 773–86.

Figure captions

Fig. 1 | Bake-reversion hardening in a metastable $Fe_{45}Mn_{35}Co_{10}Cr_{10}$ HEA: (a) EBSD phase map of undeformed microstructure corresponded with EDS elemental mapping; (b) engineering stress-strain curves of as-homogenized and bake-reversion treated HEA with strain hardening rate plot inserted; (c) comparison of strength-cumulative ductility synergy between a conventional bake-hardenable Fe-based alloy [16] and the present HEA undergoes bake-reversion hardening.

Fig. 2 | EBSD maps of phase constituent evolution with respect to increasing local strain level (with IQ value overlapped): (a1)-(d2) deformed state; (a2)-(d2) same regimes after 200 ^{o}C, 20 min reversion annealing.

Fig. 3 | Quantitative assessment of the reverse transformation: (a) phase constitution evolution before and after bake-reversion annealing (dark blue lines: FCC-austenite, orange lines: HCP-martensite); (b) average geometrically necessary dislocation (GND) density versus local strain level within the FCC-austenite (an FCC lattice constant of 3.61 Å measured from synchrotron X-ray diffraction was adopted for the GND density computation).

Fig. 4 | Kinetic features of the reverse transformation: (a) DSC curves at multiple heating rates; (b) measured A_s and A_f temperatures as a function of increasing heating rate.

Fig. 5 | Microstructural characterization of the multi-variant configuration: (a) EBSD IPF map taken at a deformed specimen after reversion treatment (local strain level ~0.30, with IQ value overlapped); (b) phase map correspond to (a); (c) and (d) ECCI micrographs for defect characteristics of regimes A and B marked in (a) and (b) (SF: stacking fault).

Fig. 6 | Kinematic-energetic model for secondary HCP-variant formation and the corresponding strengthening and ductilization mechanisms: (a) internal stress field generated by an emissary dislocation at the original FCC/HCP phase boundary; (b) energy landscape of dislocation-assisted secondary HCP-variant formation (y-axis can also be regarded as generalized stacking fault energy [29,30]); (c1)-(c4) phenomenological model elucidating the mechanisms of bake-reversion hardening.